Science Advances

AAAS

advances.sciencemag.org/cgi/content/full/3/12/eaao5496/DC1

Supplementary Materials for

One-step volumetric additive manufacturing of complex polymer structures

Maxim Shusteff, Allison E. M. Browar, Brett E. Kelly, Johannes Henriksson, Todd H. Weisgraber, Robert M. Panas, Nicholas X. Fang, Christopher M. Spadaccini

Published 8 December 2017, *Sci. Adv.* **3**, eaao5496 (2017)
DOI: 10.1126/sciadv.aao5496

This PDF file includes:

Supplementary Materials and Methods

Optical layout details and generation of holographic phase masks

The shaping of light fields using digital holography via phase-only spatial light modulators (SLM) has been extensively explored for optical trapping (*35*, *36*), 3D holographic displays (*37*, *38*), optogenetics (*39*), and to a lesser extent lithographic structure formation (*40*). The key advantage of holography for the present application is dynamic focus adjustment without changes to the optical layout. However, in the present implementation, the depth of focus at the build volume is sufficiently long such that focus adjustment of the component beams is not required. In addition, diffraction-based image projection efficiently redistributes available beam power to all image areas with bright pixels (rather than some pixels being dark). It's important to note that it is the summed intensity of the overlapping beams that polymerizes the resin. Although interference is taking place within the resin (the illumination source is coherent), the phase of each beam is uncontrolled (random), as the optical field is optimized for a specific intensity distribution. Therefore, the interference effects result in 3D speckle, and are averaged out by rapidly cycling CGHs on the SLM.

The source laser (532 nm CW, 6W maximum power, Verdi V-6, Coherent, USA) is expanded (4f1, 4f2 and 4f3 in Fig. 1) and spatially filtered (SF in Fig. 1) such that the SLM (PLUTO-VIS, Holoeye GmbH, Germany) with diagonal of 17.6 mm is illuminated by a Gaussian beam with a $1/e^2$ diameter of approximately 20 mm. The SLM itself is a 1920×1080 array of 8 μm square liquid crystal pixels, with each pixel acting as a tunable linear phase retarder between 0 and approximately 2π, driven by 8-bit image data (256 gray levels). The phase pattern $\phi_{SLM}(x, y)$ displayed on the SLM is typically referred to as a computer-generated hologram (CGH). This diffracts to form the desired intensity patterns $I_{HP}(x, y)$ when Fourier-transformed by a lens (designated FTL in Fig. 1) as

$$I_{HP}(x, y) = |E_{HP}(x, y)|^2$$

where

$$E_{HP}(x, y) = \mathcal{F}\{E_{SLM}(x, y)\} = \mathcal{F}\left\{A_{SLM}(x, y)e^{-i\phi_{SLM}(x,y)}\right\}$$

In these expressions *E* is a complex-valued electric field with amplitude *A* and phase ϕ, *I* is the intensity or irradiance of that field, and $\mathcal{F}\{\ \}$ is the Fourier transform operator.

The CGH phase patterns necessary to project the desired intensity are calculated by the iterative Gerchberg-Saxton algorithm (*41*), typically yielding sufficiently high quality reconstructions after 15-20 iterations. To eliminate interference from un-diffracted light, the calculated phase patterns have an additional phase curvature added to them, which digitally refocuses the desired intensity image to a plane (HP – hologram plane in Fig. 1) beyond the natural focal plane of the Fourier-transform lens (FTL in Fig. 1), and a beam block (BB in Fig. 1) prevents propagation of un-diffracted light. A final pair of lenses (4f4) image-relays the intensity pattern at HP to the resin cuvette and its 45° mirrors. Finally, to control speckle-induced spatial noise, many copies (generally at least $60 \cdot t_{opt}$) of each phase mask $\phi_{SLM}(x, y)$ are generated for each target image using different initial random phase distributions, producing "stacks" of images with uncorrelated digital noise. When sequentially displayed on the SLM at its maximum frame rate of 60 Hz, the spatial noise of the resulting image is reduced proportionally to the square root of the number of CGHs in the stack.

The speckle size scale is equivalent to the diffraction-limited spot size addressable by the SLM, which is ~15 and 30 μm for the x- and y-directions of our SLM, respectively, due to different SLM pixel counts. The O_2 diffusion timescale for these dimensions is ~25-100 ms, comparable to the SLM update timescale of 17 ms, so the response of the resin is just fast enough to show some of the speckle structure, rather than completely "smearing" it out. This is therefore the major contributor to the surface roughness of the fabricated parts.

In addition to attenuation compensation in mutually orthogonal beams (discussed in the next section), a non-ideality that must be overcome is inherent illumination nonuniformity due to diffraction-based image projection. In phase-modulated SLM-based holography, this arises from vignetting due to convolution of the reconstructed pattern with the single-pixel's Fourier transform (a 2D sinc^2 envelope) (*42*). To generate a compensation function, the shape of the sinc^2 envelope is recorded by projecting a CGH calculated for a uniform- intensity image, measuring the actual output, and calculating an inverse function. This intensity compensation pattern is then applied to all target images prior to calculating CGHs. When an intensity-modulated SLM (amplitude-only LCoS, or DMD micromirror), is used for pattern generation, nonuniformities in the illumination field incident on the SLM must likewise be compensated.

Calculation of cure energy doses and mutual compensation of orthogonal beams

The absorbed energy dose within the cure volume is derived by the following procedure. The average power P_B [mW/cm^2] incident on the cuvette from each of the three image subcomponent beams is measured using an optical power meter. This value of P_B is how the curves of Fig. 3B in the main text are identified. A dark region between image features is similarly

measured to account for background illumination scattered due to diffractive inefficiencies. From these an estimate of irradiance I_0 [mW/cm^2] at the cuvette wall in white pattern areas can be calculated. This irradiance value I_0 is given as the x-axis of fig. S1.

The light attenuation due to the photoinitiator as a function of the penetration depth *z* is given by the Beer-Lambert law $I(z) = I_0 e^{-2.3 \cdot \varepsilon [PI] z}$ where ε is the molar extinction coefficient, and $[PI]$ is the photoinitiator concentration. This same analysis applies for the *x* and *y* coordinates, so we carry it out here only as a *z* dependence, but when calculating multibeam superposition, the attenuation in all three directions is taken into account.

In resins with a single absorbing component, such as the one used here, the absorbed irradiance per unit volume at depth *z* is given by

$$I_{abs}(z) = \frac{dI(z)}{dz} = 2.3\varepsilon[PI] \cdot e^{-2.3 \cdot \varepsilon [PI] z} \; I_0 = a_V(z) I_0 \; ,$$

where the depth dependent pre-factor modifying the incident irradiance I_0 is lumped into a single "volumetric absorption factor" $a_V(z)$ with units of inverse length appropriate for multiplying by the area-normalized irradiance.

When working with photoinitiators for which the molar extinction coefficient isn't readily available, the resin absorbance

$$A = -\log_{10}(I/I_0) = \varepsilon[PI]z$$

is readily measured in a spectrophotometer, since cuvette path lengths are known with high precision. The resin is then simply characterized by a single key parameter; namely, its absorption coefficient $\alpha = \varepsilon[PI]$ (units of inverse length). The depth-dependent intensity $I(z)$ and the volumetric absorption factor $a_V(z) = 2.3\alpha \cdot e^{-2.3\alpha z}$ are shown in fig. S2A and B for a range of values of the absorption coefficient α.

From calculating the variation of the volumetric absorption coefficient a_V in 3D space due to 3-beam superposition (fig. S2A-C), we derive an in-plane compensation gradient for each of the three image subcomponent beams. Applied to the projection for the test-cube exposure, an example is shown in the right inset of Fig. 2A in the main text. The sub-image intensities are adjusted to maximize uniformity of the peak 3-beam absorption factor. This uniformity parameter, as shown in fig. S2D, is evaluated by calculating the relative standard deviation (RSD – standard deviation as a percentage of the mean value) of a_V values in the white-boxed strut areas indicated in fig. S2C. Without compensation, only resins with $\alpha < 0.1$ cm^{-1} have an RSD

uniformity < 3.5% which is approximately the maximum that allows successful fabrication of volume-at-once struc-tures. With compensation, this range is raised to α = 0.5 cm^{-1}, significantly widening the usable process window for the volumetric approach. The line profiles of $a_V(x)$ (i.e. the volumetric absorption coefficient variation along a single dimension) at varying locations in *y* and *z* show how the energy absorption varies for α = 0.1 cm^{-1} in fig. S2E and α = 0.5 cm^{-1} in fig. S2F, which represents the upper end of usable resin absorbance.

The actual volumetric energy dose delivered to 3-beam regions for a given experiment is estimated as $E_{CURE} = a_V(x,y,z)I_0 t_{EXP}$, where t_{EXP} is the exposure time.

Finite element photopolymerization reaction-diffusion model

The evolution of species transport and photopolymerization are described by a set of reaction-diffusion partial differential equations that incorporate the essential reactions: initiation, propagation, termination, and inhibition. In initiation, the photons absorbed by the initiator produce primary radicals which then react with the monomer to form a unit chain radical. Further reaction of these chain radicals with monomer extend their length during the propagation step. Chain growth is arrested during termination, in which two chain radicals combine to form one or two dead chains (bimolecular termination by recombination or disproportionation, respectively). Other types of termination mechanisms are not considered. Finally, molecular oxygen inhibits the polymerization by combining with chain (or primary) radicals to produce an inactive chain. The general form for the evolution of species concentration U_i is

$$\frac{\partial U_i}{\partial t} = \nabla(D_i \nabla U_i) + S_i$$

where the concentration terms U_i include the monomer [*M*], photoinitiator [*PI*], primary radicals [*R*], chain radicals [*P*], and oxygen [O_2], and the D_i are their respective diffusivities. The source term has the form

$$S_i = k_r \begin{cases} \prod_{j \in \text{products}} U_j^{c_{jr}}, & i \in \text{products} \\ 0, & \text{otherwise} \end{cases} - k_r \begin{cases} \prod_{j \in \text{reactants}} U_j^{c_{jr}}, & i \in \text{reactants} \\ 0, & \text{otherwise} \end{cases},$$

where the c_{jr} are the stoichiometric coefficients for species *j* in reaction *r*. The initiation rate coefficient is $k_{init} = R_{init}/[PI]$ (normalized to be independent of concentration), where $R_{init} = \varphi\, I_{abs}/N_A h\nu$, as defined in the main text, and I_{abs} is defined in the previous section. For the remaining rate coefficients, we incorporate the free-volume-dependent formulations from

Goodner *et al*. (*21*). Because of the temperature dependence in the kinetics and diffusion models, an energy equation with the enthalpy of polymerization is also required.

Our approach here is adapted from a microstereolithography model with a 1,6-Hexanediol diacrylate (HDDA) resin, for which the propagation and termination coefficients and the free volume parameters were determined via least-squares optimization to match the polymerization rate calculated from real-time-FTIR measurements. This resin formulation is similar enough to capture the correct physics of the PEGDA 250 resin used for experimental measurements in this work. To better match its actual kinetics, the model was tuned with a subset of the experimental induction time data by adjusting the oxygen concentration and diffusivity.

To solve the system of equations, we implement them in the COMSOL Multiphysics finite element software. To minimize the computational cost, we restrict the simulations of the cube structures to one quarter of the plane defined in Fig. 3A, relying on the mutual beam compensation to achieve approximate symmetry in the other quarters of the plane (see fig. S4). However, the 2D simulations include photon intensities from all three beam directions. For the model, we define the induction time when the average degree of polymerization within the cube strut features reach a value of 0.3 (considered equivalent to the gelation time – c.f. definitions and discussion of t_{G3} and t_{G2} in the main text). An example result in fig. S4 shows both the light intensity field (in mol/m^2/s) and fractional conversion at the induction time of 4.2 s for a resin containing 0.1% photoinitiator and 20 mW power in each beam. The rounded shape of the cured region is a result of O_2 inhibition and the finite contrast ratio of the projected optical pattern.

We computed induction/gelation times for 3-beam overlap regions with the same [*PI*], strut size, and laser power parameters as the experimental measurements to which they are compared in Fig. 2B. For [*PI*] = 0.08-0.2%, the average difference is 10%, providing validation for the model within this parameter space. When [*PI*] is lower (i.e. 0.05%, comparable to the initial oxygen concentration), cure times are under-predicted by the model (by 30-50%, data not shown), because operation in this transition region is highly sensitive to the relative concentrations of O_2 and photoinitiator. Correctly predicting O_2 inhibition in this regime remains a topic under investigation. However, as the experimental data also suggest, these model results confirm that, for the success of this fabrication technique, and its ability to produce micron-scale features, it is desirable to work at initiator concentrations elevated above the O_2 concentration.

With the validated model we explored the ability of this new manufacturing method to produce micron-scale features. Using the same cube geometry, we ran simulations with moderate laser powers and 0.1% initiator for smaller strut sizes, from 0.1 mm down to 0.025 mm. Figure S5A and D show the results for 0.1 mm and 0.025 mm, respectively. The white contour at 30% polymerization is indicative of the cross-sectional shape of the cured strut. As the feature size is reduced, the distortion increases from oxygen inhibition, radical diffusion, and a finite contrast

ratio. In fig. S5A the 0.1 mm shape is more distorted at the top and left sides, whereas the smaller feature in fig. S5D is very rounded with bulges at the lower and right sides. Two different mitigation strategies are also shown: increasing laser power to 50 mW (fig. S5B and E), and reducing O_2 concentration by an order of magnitude (fig. S5C and F). Of these two, the oxygen reduction is more successful, as evidenced by the nearly square shape in fig. S5C. The 0.025 mm shape is also significantly improved, having more symmetry and flattened edges. Also, in both mitigations, the degree of polymerization is more uniform within the contour which is desirable for robust mechanical and aging performance. Though a formal optimization of process parameters is not the focus of this work, these simulations demonstrate that under the proper conditions, micron-scale features can be manufactured.

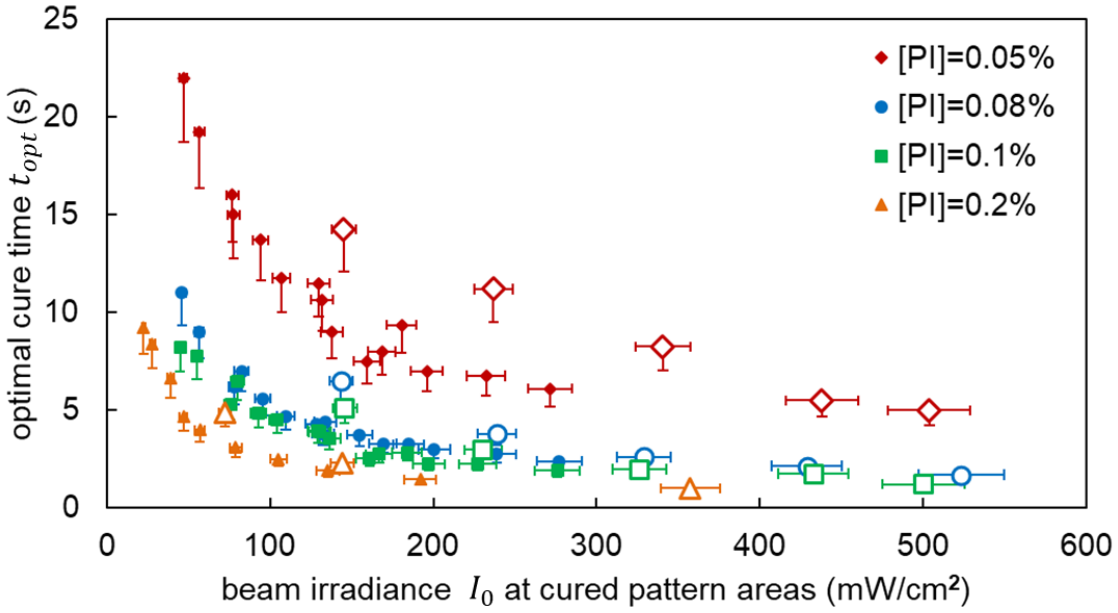

fig. S1. Experimentally measured cure times for the full range of illumination intensities. Open symbols represent data for the thinnest cube struts (0.3 mm). As discussed in the main text, the cure times for all 0.3 mm struts are extended in all cases, compared to thicker-strut timescales at identical beam irradiances. This arises from 0.3 mm struts being sufficiently thin for oxygen re-diffusion and extending the time required. At the highest irradiances, when cure times drop below 2 seconds, the 0.3 mm struts realign with the rest of the data. Vertical error bars are given one-sided due to the tendency of cure time measurements to bias upward owing to gradual resin degradation. This estimate of the data reproducibility is made as 15% of the measured value, based on N=3 replicate measurements at several representative experimental conditions. Horizontal error bars are given as 5% based on similar consideration.

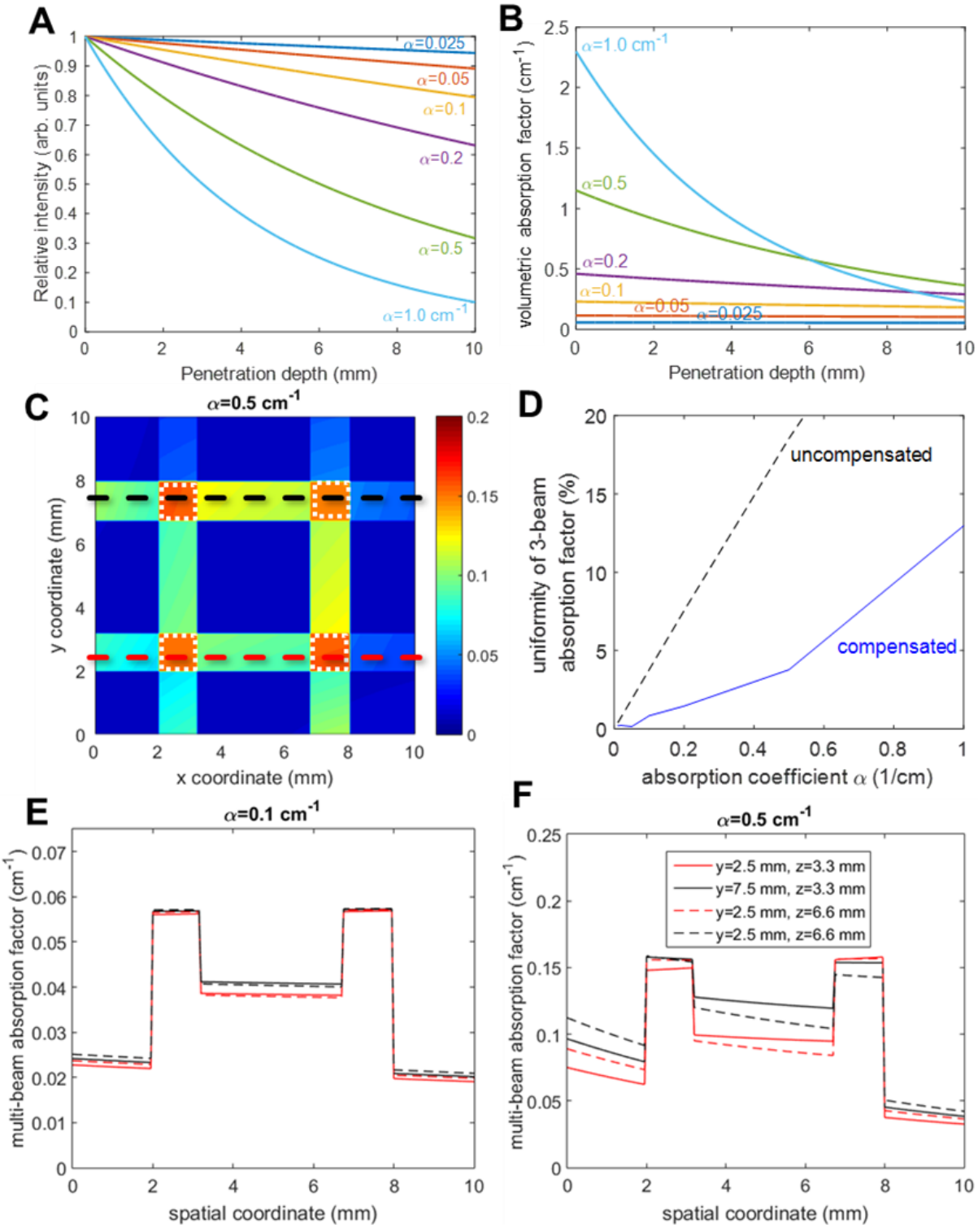

fig. S2. Details of intensity attenuation effects and compensation for resins with differing absorption coefficients. For a range of absorption coefficients $\alpha = \varepsilon[PI]$ (**A**) shows the drop-off in intensity and (**B**) shows the corresponding volumetric absorption factor a_V through the

bulk of the resin volume used in this work. Similarly to Fig. 3A, (**C**) shows a 2D plane from the 3D intensity distribution simulation, here plotted as the value of a_V at z = 5.0 mm. Panels D-F are derived from similar calculations. (**D**) shows the uniformity of peak absorption locations, boxed with white dashed lines in (C), with and without transverse intensity compensation. (**E**) and (**F**) are line-plots of compensated a_V values at the indicated y and z locations, corresponding to the black and red dashed lines in panel D. At $\alpha = 0.5\,\mathrm{cm}^{-1}$ and above, as shown in panel F, the non-uniformities can no longer be effectively compensated by linear multibeam superposition.

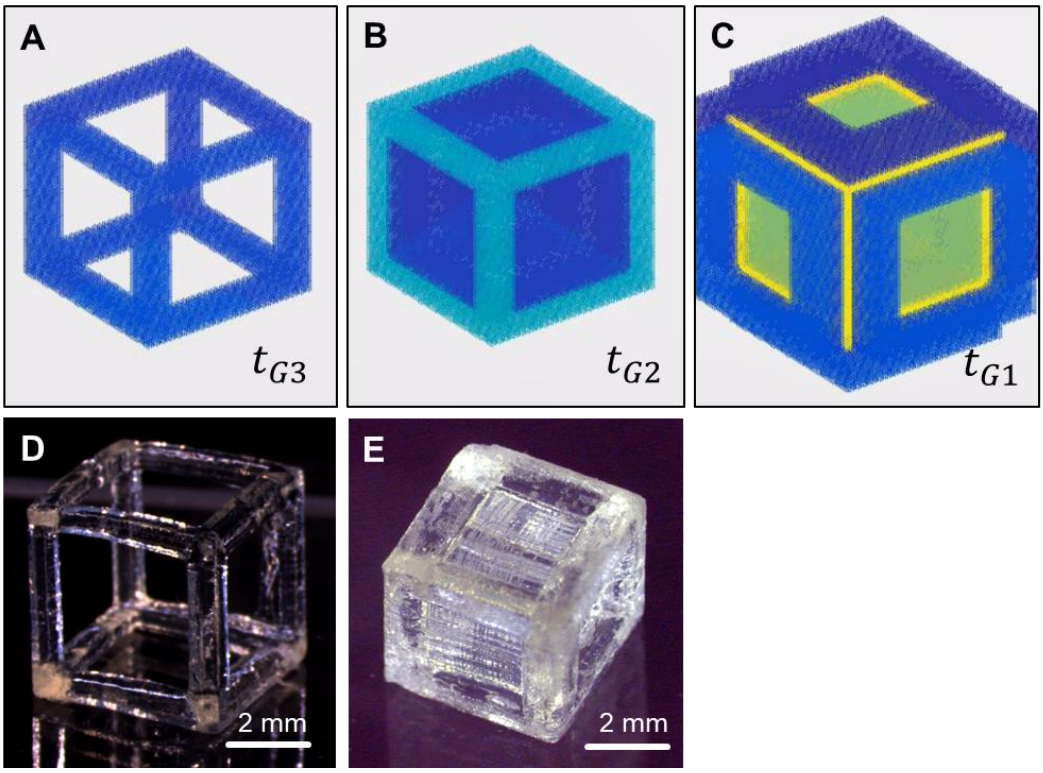

fig. S3. Progression of multibeam 3D volumetric polymerization of cube structures and eventual overcuring. (L to R) The first regions to appear are those with all three beams overlapping, representing the 3-beam gel threshold (t_{G3}). Continuing the exposure leads to the appearance of cube faces as regions illuminated by only two beams absorb sufficient energy cross the gel threshold at t_{G2}. Eventually single-beam illuminated regions also solidify t_{G1}. The top row shows a qualitative prediction of this behavior using a simple thresholding model (with color indicating degree of polymer cross-linking), with the bottom row showing experimentally observed structures. At t_{G1} structures that formed adhered to the inside of the vial, and were impossible to remove without damage, so a photo of such a part is not shown.

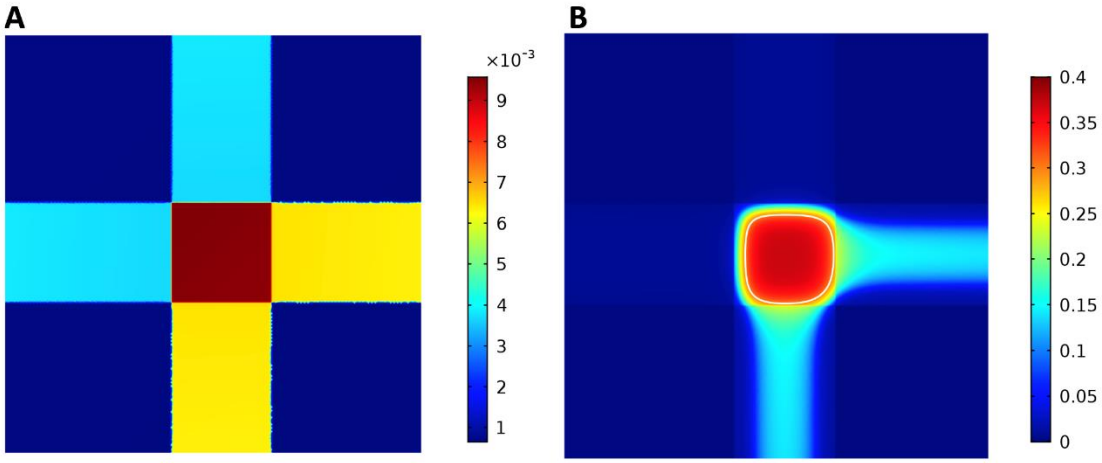

fig. S4. Representative results from the polymerization simulations. For a laser power of 20 mW, a 0.1% photoinitiator concentration, and a 1.2 mm strut size, (**A**) shows the light intensity within the resin from the three beams in mol/m^{2}s and (**B**) shows the degree of polymerization at the gel or inhibition time of 4.2 s. The images represent the entire simulation domain, corresponding to a quarter of the area in the cuvette with symmetry conditions at the left and lower edges. The white contour corresponds to 0.3 or 30% double-bond conversion and exhibits rounded corners from diffusion of oxygen and radicals.

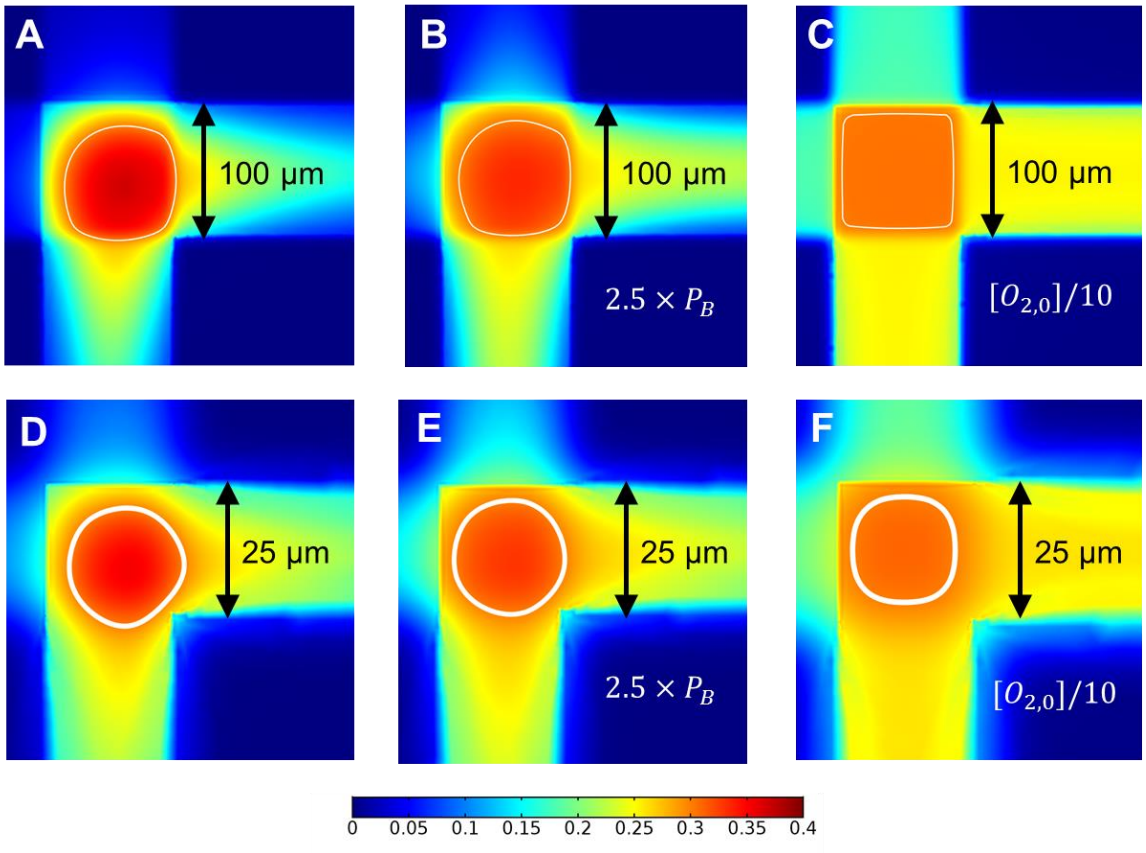

fig. S5. Effects of curing conditions on feature resolution and distortion. Polymerization fields are shown for cube strut sizes of 0.1 mm in (**A**), (**B**), and (**C**), and 0.025 mm in (**D**), (**E**), and (**F**) with [*PI*]=0.1%. This series of images also corresponds to different process parameters: in (A) and (D) incident beam power is 20 mW. In (B) and (E) the power is 50 mW, and in (C) and (F) the initial oxygen concentration is reduced by a factor of 10 and the power is 20 mW. The white contour corresponds to a 0.3 fractional polymerization and is representative of the shape of the cured part. As the strut size is reduced, the resulting cured feature becomes more distorted. In (D) the contour is significantly rounded and bulged on the right and lower sides. Both increasing the laser power and lowering the O_2 concentration mitigate this distortion. The legend at the bottom maps the colors to degree of polymerization.